Supporting Information

Nanoscale Assembling of Graphene Oxide with Electrophoretic Deposition Leads to Superior Percolation Network in Li-ion Electrodes: $TiNb_2O_7$/rGO Composite Anodes

Marianna Uceda[1a], Hsien-Chieh Chiu[a], Jigang Zhou[b], Raynald Gauvin[a], Karim Zaghib[a, b] and George P. Demopoulos[a*]

[a]Materials Engineering, McGill University, Montreal, QC, Canada

[b]Canadian Light Source Inc., University of Saskatchewan, Saskatoon, Canada

[b]Centre d'excellence-ETSE, Hydro-Québec, Varennes, QC, J3X 1S1, Canada

[1]marianna.uceda@mail.mcgill.ca

[*]Corresponding Author: **ORCID** #0000-0001-8112-5339, Email: george.demopoulos@mcgill.ca

The present document contains supplementary information regarding the solid-state synthesis of TNO, its ball-milling, carbon coating, characterization and electrochemistry. A graph showing the temperature changes during carbon-coating of TNO is given including Raman characterization of the D and G bands showing the presence of graphitic carbon. EPD suspension and parameter selection is presented to explain the necessity of high amounts of GO in the suspension and the reason for voltage selection. After annealing of the EPD coatings, thermogravimetric analysis is used to quantitatively determine the amount of rGO in the coating. Additionally, XPS of C 1s spectra is used to show the $GO \rightarrow rGO$ transformation during the annealing step. XRD patterns of the EPD coating before and after annealing are included, along with a schematic of the TNO lattice showing the planes of the main peaks observed in the XRD pattern. EDS F Kα mapping of the PVDF electrode cross-section is given to show the cracking observed for the 18 wt.% rGO PVDF electrode and the dispersion of the fluoropolymer binder. The final section includes cyclic voltammograms of an electrode composed of 80/20 wt.% rGO/PVDF at varying scan rates to show the current response of pure rGO. Additionally, the voltammograms of the EPD and PVDF electrodes (10 and 18 wt.% rGO) at varying scan rates are also included along with the analysis used to study pseudocapacitive contributions from rGO, these include 1) plots of the log of peak cathodic current vs. log of scan rate and 2) plots of $i(V)/v^{0.5}$ vs $v^{0.5}$.

1. TNO Synthesis and Carbon-Coating

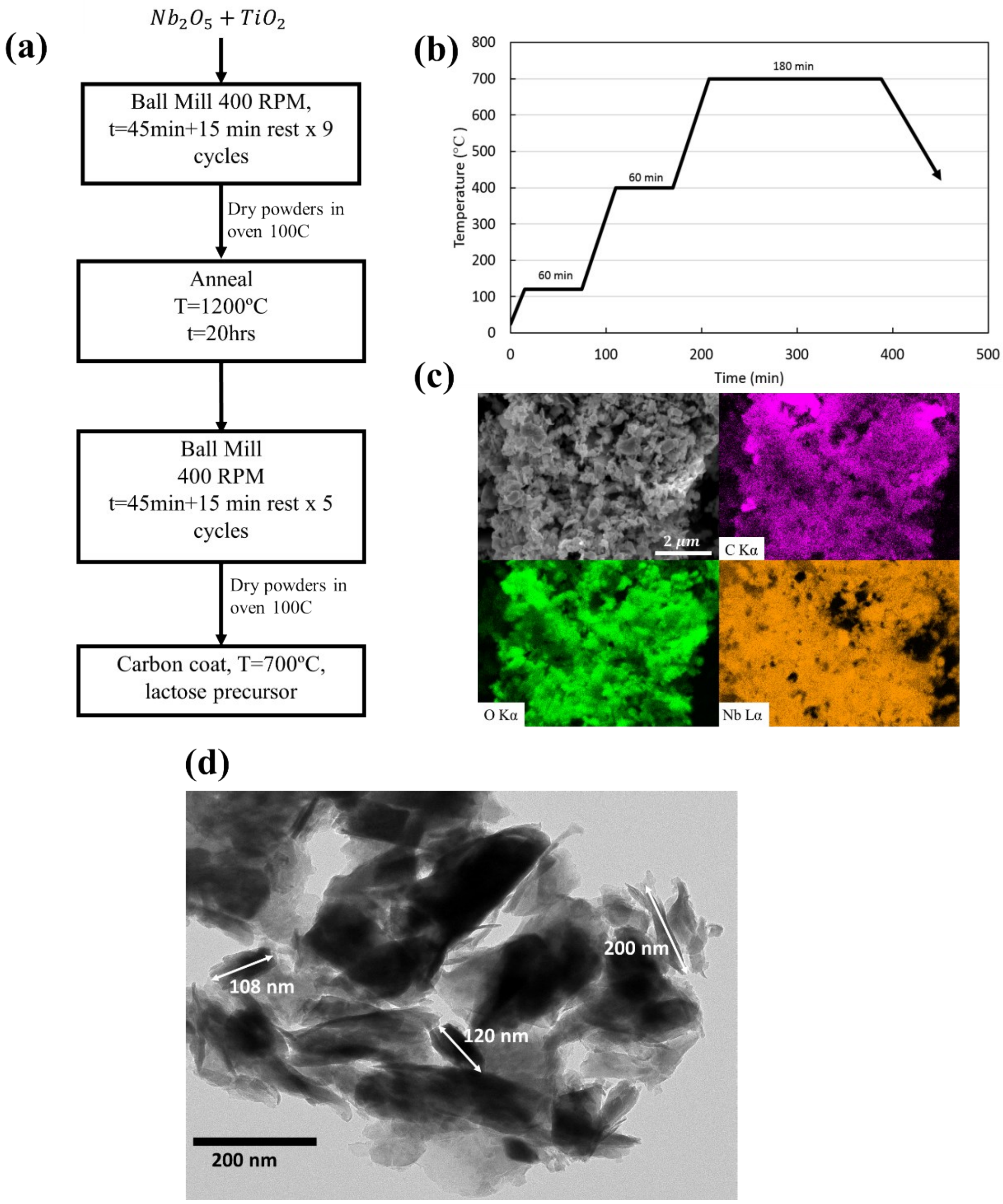

Figure S1: (a) Solid-state synthesis flowchart for ball-milled and carbon-coated TNO,(b) carbon-coating temperature profile, (c) EDS characterization of the carbon-coated/ball-milled (CCBM) material showing the SE image and respective C, O, and Nb maps, and (d) TEM image of the CCBM

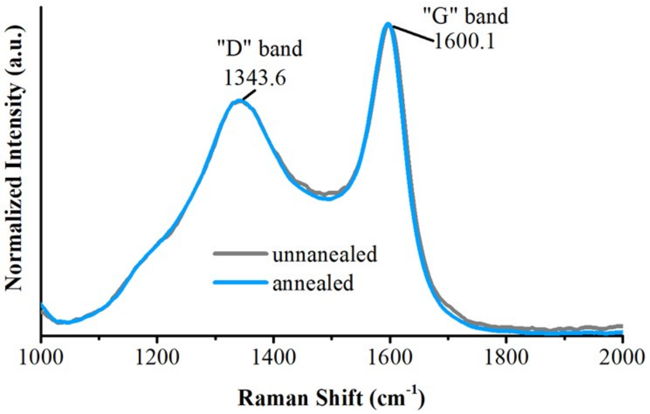

Figure S2: Raman spectra for ball-milled carbon-coated TNO powders before (“unannealed”) and after (“annealed”) high temperature annealing to reduce rGO.

Raman characterization in Figure S2 confirms the carbon-coating through the appearance of the characteristic “D” and “G” bands which are the defect and graphitic bands respectively. [1] The high temperature (600 °C) annealing performed to effect GO reduction in the EPD electrodes is shown to have no effect on the peak position or intensity of the defect and graphitic bands implying it does not degrade in any way the carbon-coating.

2. Ball-milling effect on electrochemical performance

The initial high capacity followed by a rapid drop is characteristic of the ball-milled material as the pristine material shown in Figure S3 does not exhibit the same behavior. This initially high capacity is attributed to the small particle size minimizing the lithium diffusion length. However, the rapid and irreversible capacity has been associated to structural disordering induced by ball-milling. [2] While the degradation/disordering is not desirable, the ball-milling and size reduction of these particles is necessary. Cyclic voltammetry for the pristine TNO (with carbon black) shown in Figure S3 shows broad peaks and severe polarization – as a result of the large particle size and Li^+ diffusion lengths. [3] When compared to the pristine material, ball-milling had positive effect on the initial performance. As seen in in Figure S3, the resulting voltammogram for the carbon-coated ball-milled material with carbon black shows the Nb^{5+}/Nb^{4+} redox couple dominant peaks at 1.62/1.67 V vs. Li^+/Li, shoulders at 1.57/1.47 V, which arise from the different positions of Nb atoms (of edge- or corner-shared octahedra). The broad peaks at 1.79/1.93 V and 1.4/1 V correspond to Ti^{4+}/Ti^{3+} and Nb^{4+}/Nb^{3+} redox couples respectively. [4] However, prolonged cycling showed rapid deterioration within the first 10 cycles.

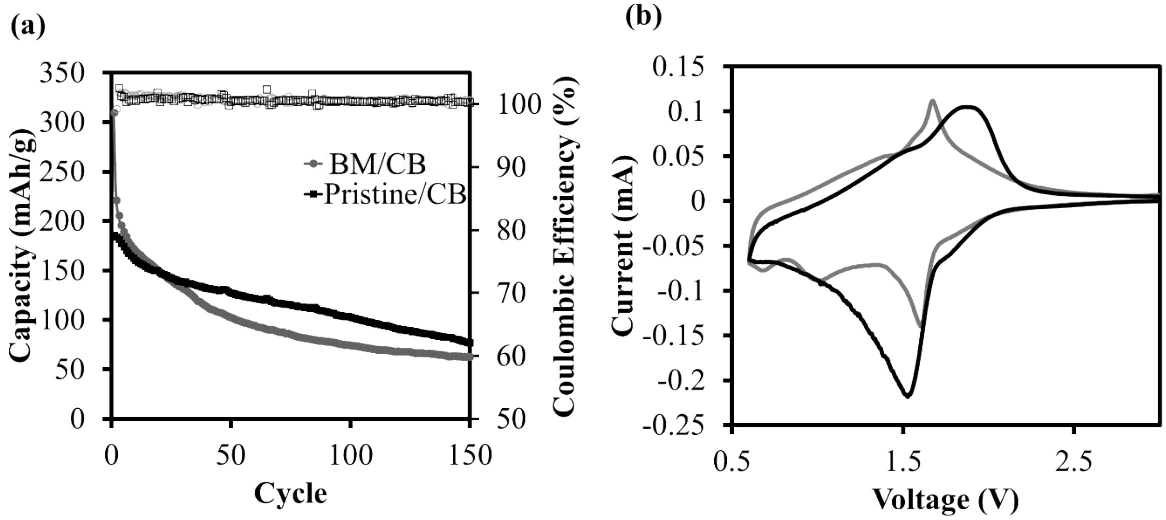

Figure S3: (a) Cycling at 0.5C and (b) 0.1 mV/s CV from 0.5 to 3 V vs. Li^+/Li of the PVDF electrodes with carbon black as conductive additive using pristine material ("Pristine/CB") and milled material ("BM/CB").

3. EPD Suspension and Parameter Selection

In this system that features GO, ethanol was found to be a suitable medium for preparing a stable TNO suspension as determined in our previous work. [5] Pure GO and TNO in suspension yield a zeta potential of -28 mV and -18 mV respectively. A mixture of 90/10 wt.% TNO/GO gave a zeta potential of -29 mV, however increasing the GO content to 30% lowered the zeta potential to -15 mV. The low GO suspension yielded a poor deposit due to a low current response when 30V was applied for ten 15s stages (see Figure S4), however increasing the amount of GO led to a drastic increase in current response and visible improvement of deposit quality using the same conditions. The poor deposit quality of the low GO suspensions is attributed to the higher colloid stability which makes it difficult to overcome the interparticle distance (needed for deposition to occur) without increasing the voltage. However, at lower zeta potentials this barrier is lower.

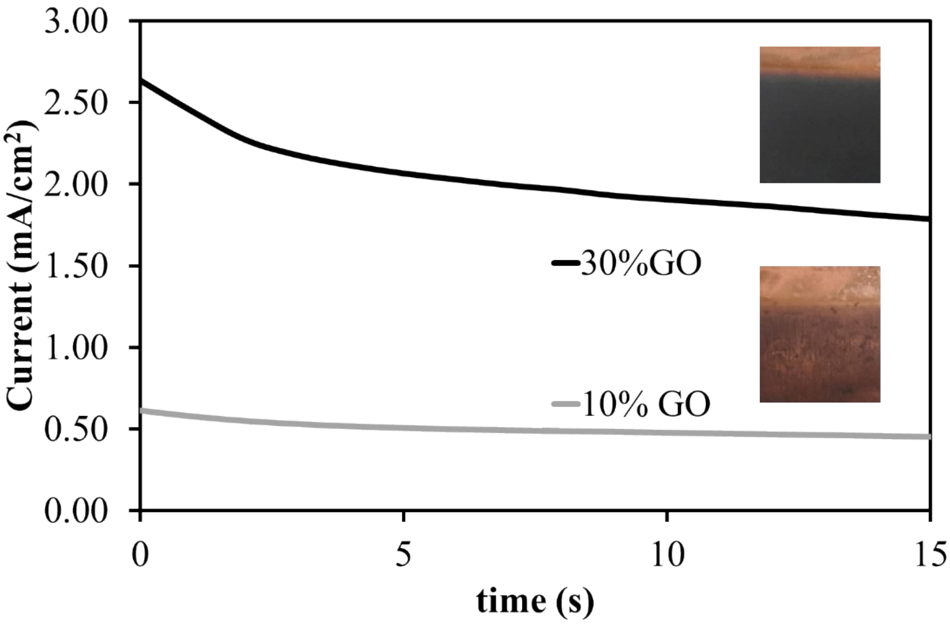

Figure S4: Current response for varying suspension quantity of GO with achieved deposit (on copper substrate) after ten 15-second deposition stages.

The voltage was maintained at 30V in an attempt to mitigate the oxidation, and subsequent redeposition, of copper. However, some faint copper deposits are still observed through cross-sectional EDS and XPS of the untreated and annealed EPD electrodes (Figure S5). The XPS of Cu 2p shows peaks belonging to Cu/Cu^+ at 932 and 952 eV (for 2p 3/2 and 1/2 respectively) and Cu^{2+} peaks at 934 and 954 eV (for 2p 3/2 and 1/2 respectively). They are present before and after annealing although the annealing stage removes some of the Cu^{2+}, as the result of reduction under H_2 atmosphere.

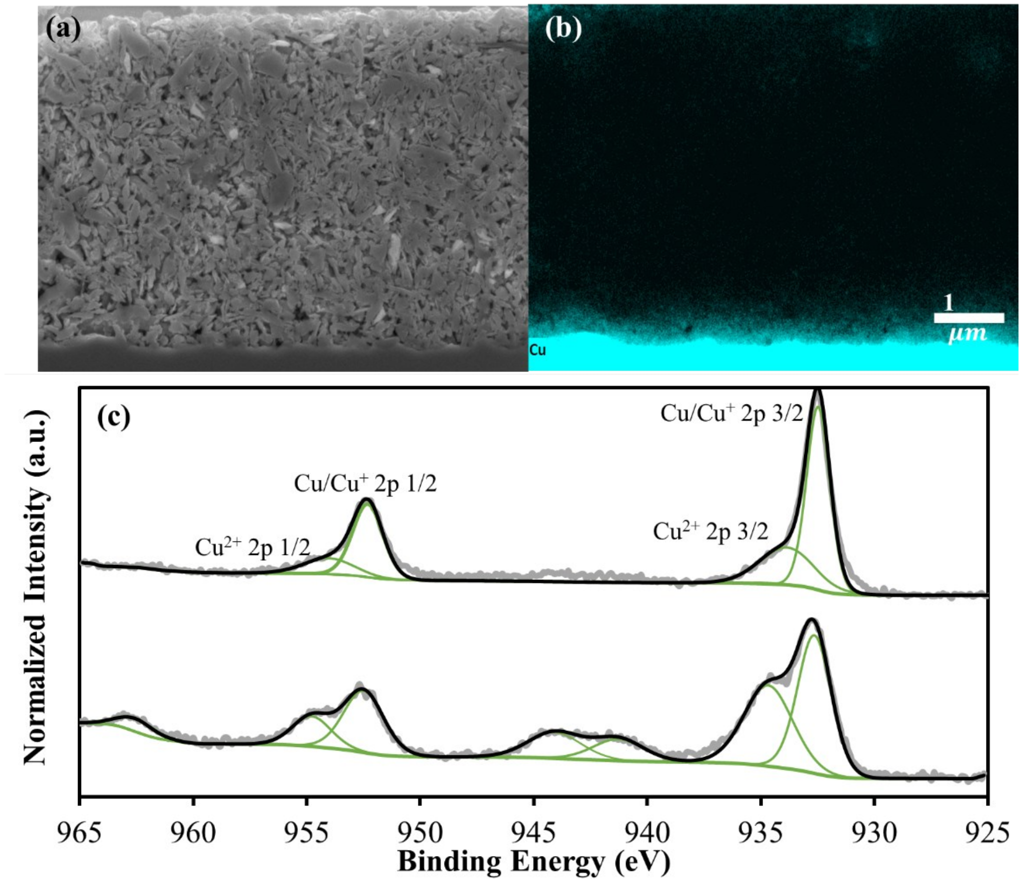

Figure S5: (a) Cross-sectional SE image and (b) EDS of Cu Lα of EPD annealed electrode; and (c) XPS of Cu 2p for (bottom) non-annealed and (top) annealed EPD electrode.

4. TGA of EPD Annealed Electrode

Figure S6 shows the TGA results, along with the corresponding derivative thermogravimetry curves (DTG), for the carbon-coated ball-milled TNO (BMCC) and the annealed EPD (TNO/rGO) electrode. The DTG peaks indicate the point of maximum rate of mass loss.

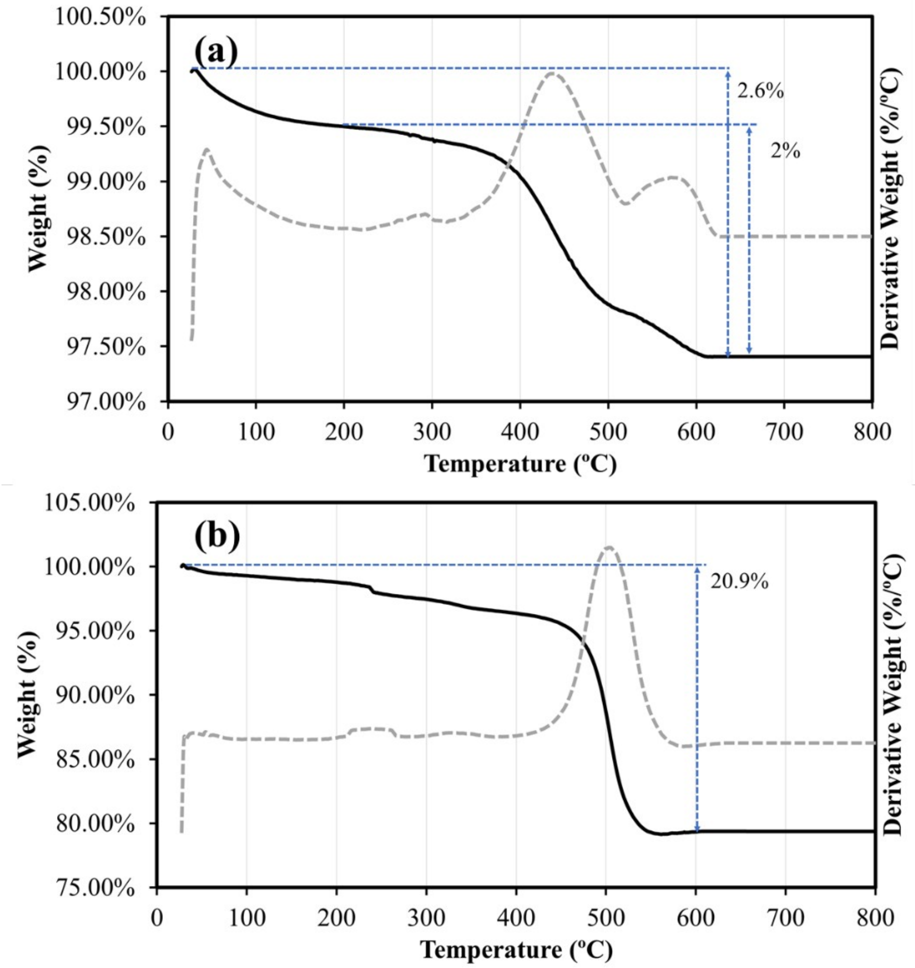

Figure S6: TGA of (a) carbon-coated ball-milled TNO and (b) annealed EPD TNO/rGO electrode.

The TGA results for the ball-milled carbon-coated material (see Figure S6 a) shows an initial weight loss of 0.6 wt.% prior to 200 °C which is attributed to moisture. The loss occurring between 200 – 600 °C is considered to be from the decomposition of the carbon-coating and accounts for ~2 wt.%. Similarly, mass lost prior to 200 °C for the EPD electrode (see Figure S6 b) is attributed to moisture loss. A sharp increase in mass loss at around 400 °C indicates the volatilization of some groups associated with rGO in the composite electrode, the total amount of rGO is found to be around ~18 wt.%.

5. XPS of C 1s

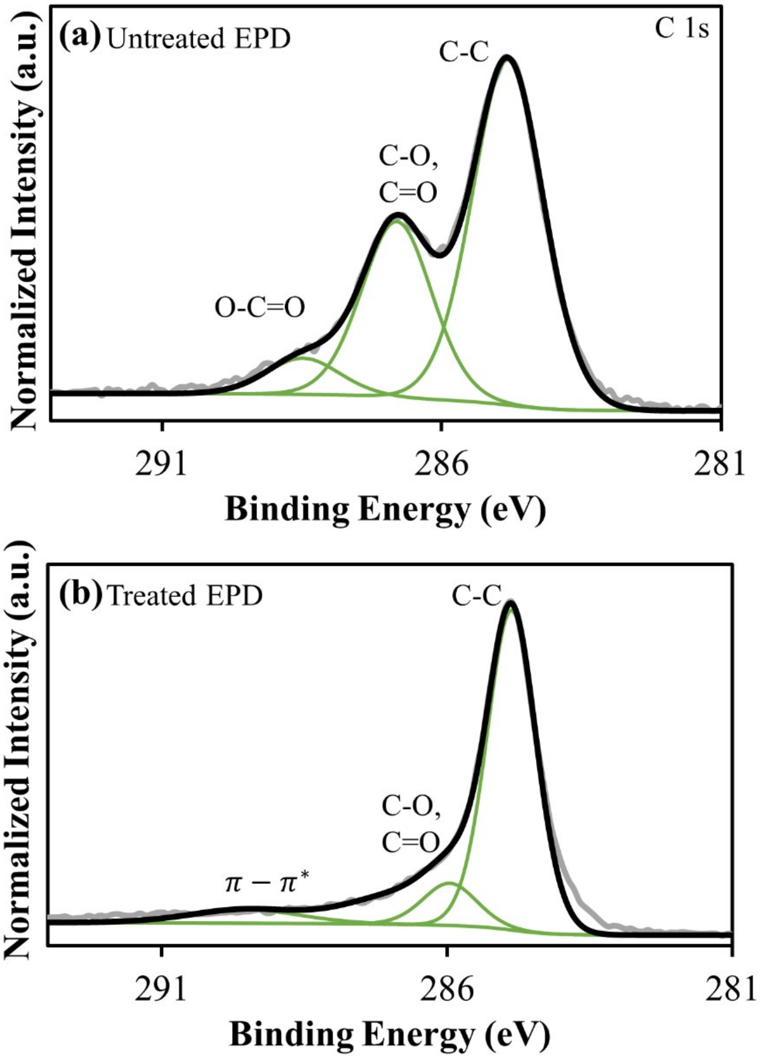

Figure S7: C 1s spectra for (a) untreated (as formed through EPD prior to annealing) and (b) treated (i.e. annealed at high temperature) EPD coating.

6. TNO Structure Schematic and XRD

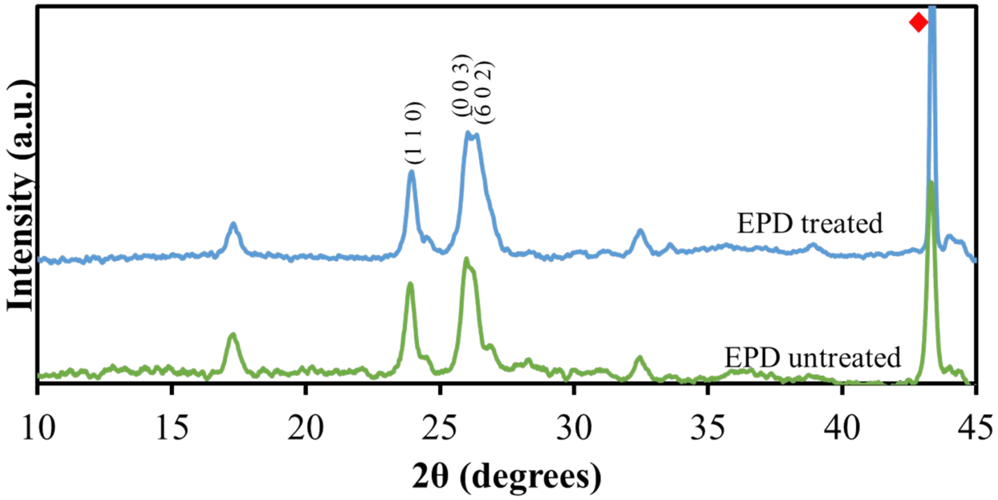

Figure S8: XRD pattern for the EPD electrode before and after annealing with ♦ denoting the presence of the Cu substrate.

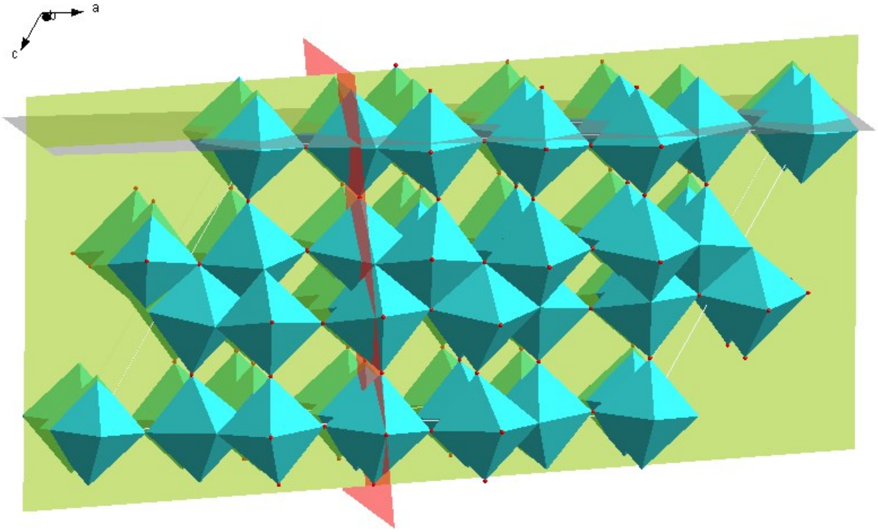

Figure S9: TNO structure where the inserted lattice planes are: green (110), purple (003) and red ($\bar{6}$02). The cyan-colored octahedra consist of the transition metals Ti and Nb at the center with the red dots representing oxygen atoms.

7. PVDF Fluoride Maps

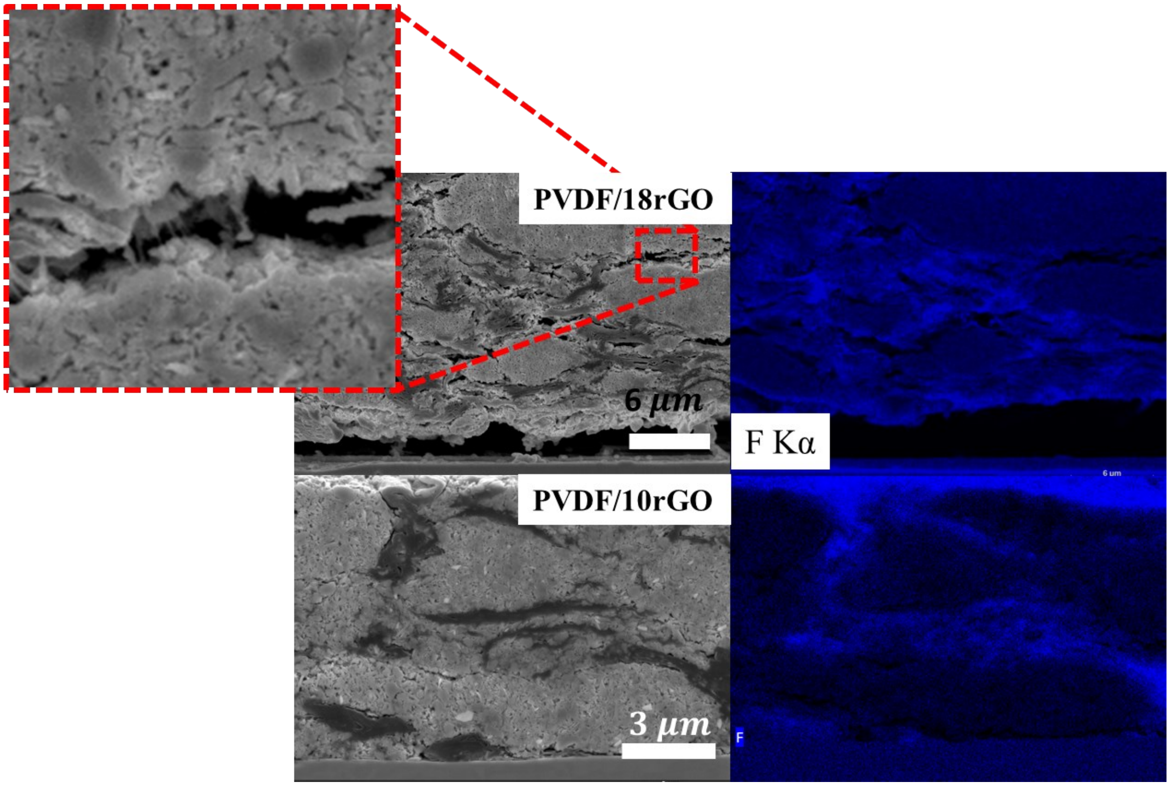

Figure S10: Cross-sectional SEM images of the PVDF/18rGO and PVDF/10rGO with corresponding F Kα showing PVDF binder dispersion.

8. Cyclic Voltammetry and Pseudocapacitance

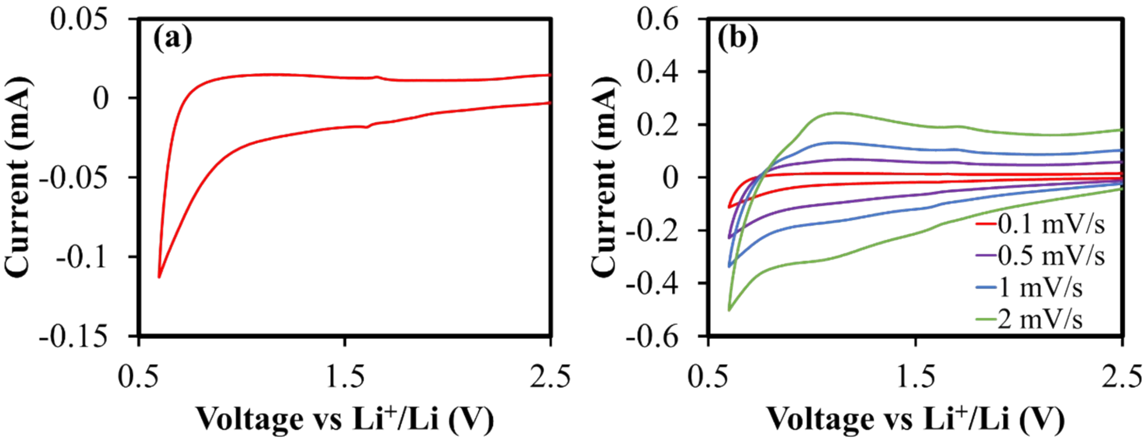

Figure S11: Cyclic voltammetry for rGO/PVDF 80/20 wt.% electrode at (a) 0.1 mV/s and (b) at varying scan rates 0.1-2 mV/s.

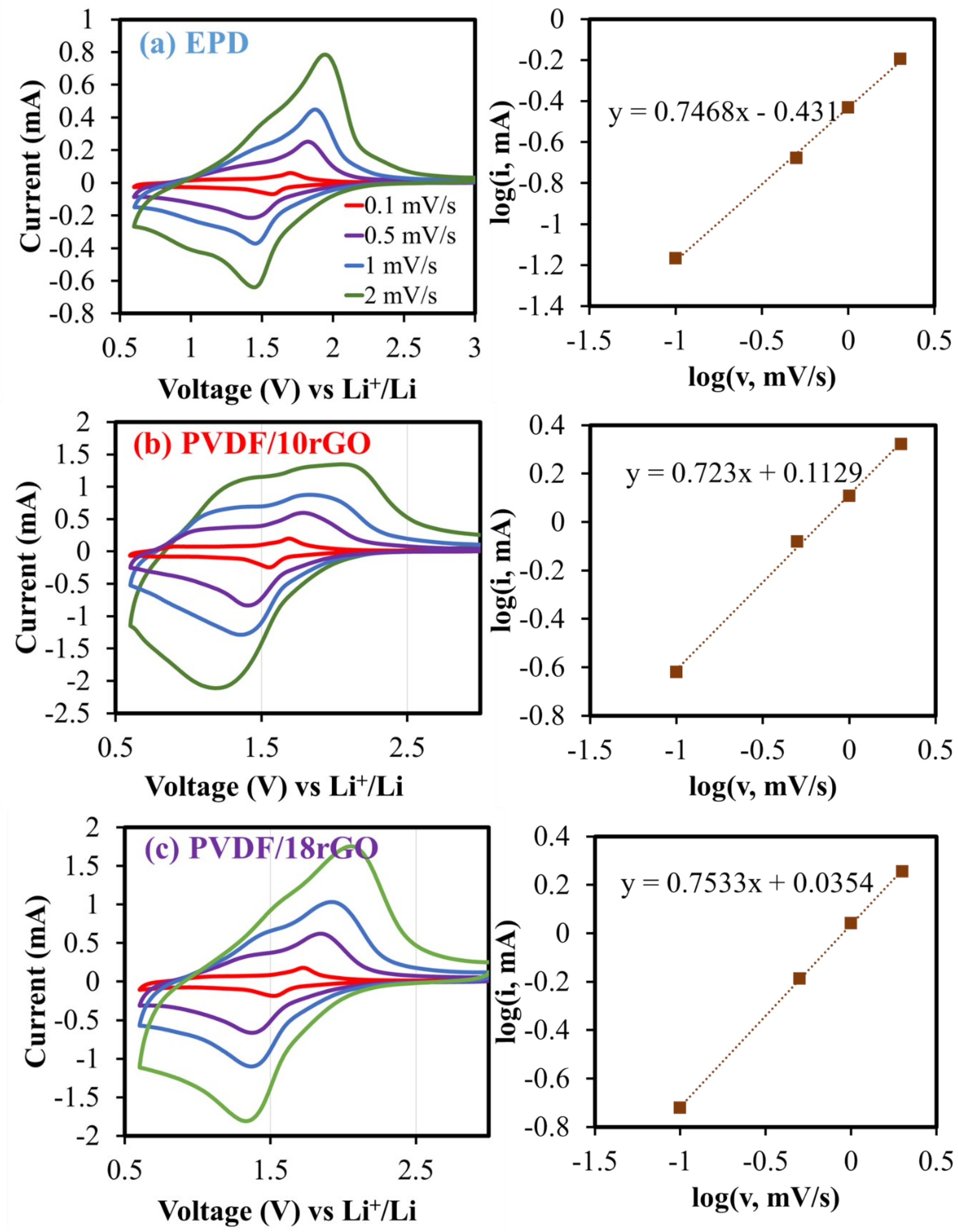

Figure S12: Cyclic voltammetry at increasing scan rate for (a) EPD/rGO, (b) PVDF/10rGO, and (c) PVDF/18rGO electrodes along with the plotted log of peak cathodic Nb^{5+}/Nb^{4+} current vs. log of sweep rate.

The pseudocapacitive contribution to the current response $i(V)$ can be calculated using the following equation [6–8]:

$$i(V) = k_1 v^{0.5} + k_2 v$$

Where $k_1 v^{0.5}$ and $k_2 v$ are the current contributions stemming from surface capacitive effects and diffusion-controlled intercalation respectively. The constants k_1 and k_2 can be determined at fixed potential (V) values by varying the scan rates (v). A plot of $i(V)/v^{0.5}$ vs. $v^{0.5}$ will yield k_1 and k_2 from the y-intercepts and slopes respectively. This calculation was performed on the EPD, PVDF/10rGO, and PVDF/18rGO and showed that the relationship was not linear across this voltage range. This indicates the pseudocapacitive contribution differs depending on the state-of-charge. Thus, the exact quantitative contribution from pseudocapacitance is difficult to calculate. An example of this is shown in Figure S13.

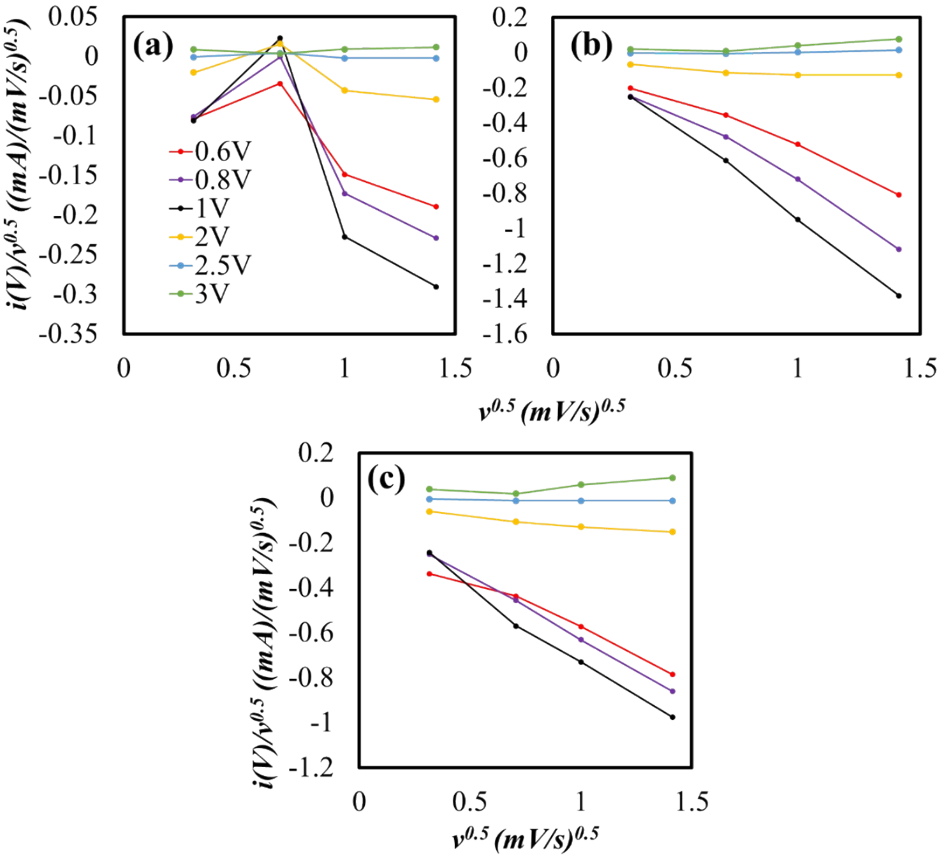

Figure S13: Correlation between $i(V)/v^{0.5}$ vs. $v^{0.5}$ for the cathodic sweep of the (a) EPD, (b) PVDF/10rGO, and (c) PVDF/18rGO electrode from 0.6V-3V at sweep rates of 0.1, 0.5, 1, and 2 mV/s showing loss of linearity at varying voltages.

9. XANES on Pristine and Cycled Lithiated Electrodes

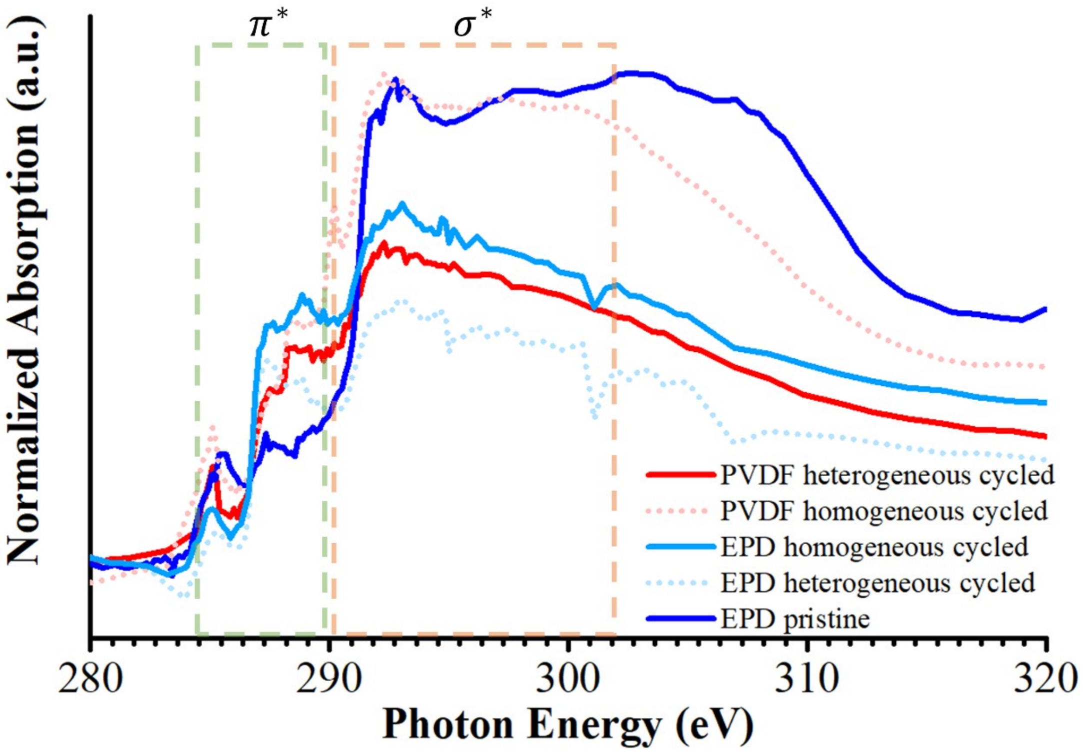

Figure S14: C K-edge XANES for uncycled EPD electrode (referred to as the "pristine" material), and cycled EPD and PVDF electrodes. The spectra are taken from "homogeneous" and "heterogeneous" zones of both EP D and PVDF electrodes. This graph reveals the "white line" intensity reduction experienced by all cycled materials with respect to the pristine material.

10. References

1 J. Schwan, S. Ulrich, V. Batori, H. Ehrhardt and S. R. P. Silva, *J. Appl. Phys.*, 1996, **80**, 440–447.

2 T. Pan, J. Alvarado, J. Zhu, Y. Yue, H. L. Xin, D. Nordlund, F. Lin and M. M. Doeff, *J. Electrochem. Soc.*, 2019, **166**, A1964–A1971.

3 Y. Wang, H. Li, P. He, E. Hosono and H. Zhou, *Nanoscale*, 2010, **2**, 1294–1305.

4 S. Lou, Y. Ma, X. Cheng, J. Gao, Y. Gao, P. Zuo, C. Du and G. Yin, *Chem. Commun.*, 2015, **51**, 17293–17296.

5 M. Uceda, H.-C. Chiu, R. Gauvin, K. Zaghib and G. P. Demopoulos, *Energy Storage Mater.*, 2020, **26**, 560–569.

6 S. Li, J. Chen, X. Gong, J. Wang and P. S. Lee, *NPG Asia Mater.*, 2018, **10**, 406–416.

7 J. Wang, J. Polleux, J. Lim and B. Dunn, *J. Phys. Chem. C*, 2007, **111**, 14925–14931.

8 S. Lou, X. Cheng, Y. Zhao, A. Lushington, J. Gao, Q. Li, P. Zuo, B. Wang, Y. Gao, Y. Ma, C. Du, G. Yin and X. Sun, *Nano Energy*, 2017, **34**, 15–25.